PAPER

Check for updates

One-pot synthesis of CoFe$_2$O$_4$/rGO hybrid hydrogels with 3D networks for high capacity electrochemical energy storage devices

Lingxia Zheng,[ab] Lingtong Guan,[a] Guang Yang,[a] Sanming Chen[ac] and Huajun Zheng [ID] *[ab]

CoFe$_2$O$_4$/reduced graphene oxide (CoFe$_2$O$_4$/rGO) hydrogel was synthesized *in situ via* a facile one-pot solvothermal approach. The three-dimensional (3D) network structure consists of well-dispersed CoFe$_2$O$_4$ nanoparticles on the surfaces of graphene sheets. As a binder-free electrode material for supercapacitors, the electrochemical properties of the CoFe$_2$O$_4$/rGO hybrid hydrogel can be easily adjusted by changing the concentration of the graphene oxide (GO) precursor solution. The results indicate that the hybrid material made using 3.5 mg mL^{-1} GO solution exhibits an outstanding specific capacitance of 356 F g^{-1} at 0.5 A g^{-1}, 68% higher than the pure CoFe$_2$O$_4$ counterpart (111 F g^{-1} at 0.5 A g^{-1}), owing to the large specific surface area and good electric conductivity. Additionally, an electrochemical energy storage device based on CoFe$_2$O$_4$/rGO and rGO was assembled, which exhibits a high energy density of 17.84 W h kg^{-1} at a power density of 650 W kg^{-1} and an excellent cycling stability with 87% capacitance retention at 5 A g^{-1} after 4000 cycles. This work takes one step further towards the development of 3D hybrid hydrogel supercapacitors and highlights their potential application in energy storage devices.

Introduction

In recent years, the conversion and storage of energy originating from green and renewable resources has becoming increasingly in demand. Supercapacitors (also known as electrochemical capacitors), as new energy storage systems, have attracted huge attention due to their fast charge/discharge rate, superior power density and long cycle life.[1–6] However, the low energy density (normally less than 10 W h kg^{-1}) has limited their commercial applications.[1,6] In the past few years, numerous researchers have already made many efforts to improve the specific capacitance by developing nanostructured electrode materials or increasing the operating voltage of supercapacitors without sacrificing their power density and cycle life.[7–11]

The electrochemical performance of supercapacitors depends mainly on the structure and properties of the electrode materials. To date, various materials such as transition metal oxides, metal hydroxides and carbon-based materials have been extensively explored.[12–19] Among them, one kind of binary metal oxide, CoFe$_2$O$_4$, has been widely used as an electrode material for lithium ion batteries and supercapacitors, due to its high theoretical specific capacitance, good chemical stability, and good electrical and magnetic properties.[20–23] However, the practical application of pure CoFe$_2$O$_4$ is limited because of its poor electrical conductivity. To address this problem, many efforts have been devoted to developing nanocomposites based on CoFe$_2$O$_4$ and carbon materials.[24–29] For instance, a ternary cobalt ferrite/graphene/polyaniline composite was prepared *via* a combination of hydrothermal and polymerization processes, and was found to exhibit a high specific capacitance of 1133.3 F g^{-1}, superior rate capability and excellent cycling stability.[24] Similarly, He *et al.* reported that the specific capacitance and cycling stability of reduced graphene oxide–CoFe$_2$O$_4$ composites synthesized using a co-precipitation method were greatly improved compared with those of the pure CoFe$_2$O$_4$ electrode.[30] Such composite materials not only can improve the specific capacitance, but also contribute to an improved rate capability. Thus, it is advantageous to introduce carbonaceous species into nanostructured CoFe$_2$O$_4$-based electrode materials to enhance their electrochemical properties.

Graphene, a typical two-dimensional (2D) one-atom-thick carbon material, has attracted considerable attention because of its appealing features including huge surface area, superb thermal conductivity, electronic conductivity, and mechanical properties.[31–35] Interestingly, Shi's group recently reported a self-assembled graphene hydrogel in a 3D network *via* a convenient one-step hydrothermal method, which exhibited good electrical conductivity, mechanical strength and thermal stability, showing promise for high performance supercapacitors.[36] Many

[a]Department of Applied Chemistry, Zhejiang University of Technology, Hangzhou 310032, China. E-mail: zhenghj@zjut.edu.cn

[b]State Key Laboratory Breeding Base of Green Chemistry Synthesis Technology, Zhejiang University of Technology, Hangzhou 310032, China

[c]College of Chemistry and Environmental Engineering, Shenzhen University, Shenzhen 518060, China

researchers have carried out intensive studies on various electrode materials based on graphene hydrogels.[37–42] For example, Wang *et al.* reported that NiOOH nanosheet/graphene hydrogel-based electrode materials, obtained *via* combined solvothermal and hydrothermal reactions, delivered a high capacitance of 1162 F g^{-1} at 1 A g^{-1} and 981 F g^{-1} at 20 A g^{-1}.[38] Zhu *et al.* assembled a hierarchical and interconnected reduced graphene oxide/β-MnO$_2$ nanobelt hybrid hydrogel *via* a hydrothermal route, which exhibited higher specific capacitance and better cycling stability than pure β-MnO$_2$ nanobelts.[39] Nevertheless, the synthesis of CoFe$_2$O$_4$ nanostructures with a self-assembled 3D graphene hydrogel composite for use in supercapacitors has rarely been reported.

Herein, novel CoFe$_2$O$_4$ nanoparticles/reduced graphene oxide (CoFe$_2$O$_4$/rGO) hybrid hydrogels were synthesized *via* a facile one-pot solvothermal method. The attachment of uniformly-distributed CoFe$_2$O$_4$ nanoparticles on the surfaces of graphene sheets is beneficial for providing more electroactive sites for faradic redox reactions. Interestingly, the CoFe$_2$O$_4$/rGO hybrid hydrogels possess a 3D mesoporous network, which can offer easy diffusion of the electrolyte and efficient pathways for electron transfer and ion transport. As binder-free electrode materials for supercapacitors, the CoFe$_2$O$_4$/rGO hybrid hydrogels exhibit excellent electrochemical performance with high capacitance, good rate capability and remarkable cycling stability. In addition, an electrochemical energy storage device was assembled, using CoFe$_2$O$_4$/rGO hybrid hydrogel as the positive electrode and rGO hydrogel as the negative electrode, and was found to deliver high energy density and cycling stability. The charming electrochemical properties demonstrate the potential application of CoFe$_2$O$_4$/rGO hybrid hydrogels in high performance supercapacitors.

Experimental section

One-pot solvothermal synthesis of CoFe$_2$O$_4$/rGO hybrid hydrogels

Graphite powder (400 mesh) was purchased from Port Co., Ltd. (Shenzhen, China). KMnO$_4$, NaNO$_3$, HCl (37 wt%), H$_2$SO$_4$ (98%) and H$_2$O$_2$ (30%) were purchased from Aladdin Industrial (Shanghai, China). All the reagents were of analytical grade and used directly without further purification in the experiments.

GO was prepared according to a modified Hummers' method.[40–43] The CoFe$_2$O$_4$/rGO hybrid hydrogel was prepared using a solvothermal method. In a typical procedure, GO powder was dispersed in 30 mL of deionized water to form a homogeneous aqueous solution (2 mg mL^{-1}). 1 mmol of Co(NO$_3$)$_2$·6H$_2$O, 2 mmol of Fe(NO$_3$)$_2$·6H$_2$O and 5 mmol of sodium acetate were dissolved into 30 mL of ethylene glycol. Then the above solutions were mixed together and vigorously stirred for 1 h. Subsequently, the mixed solution was transferred into an 80 mL Teflon-lined stainless-steel autoclave and kept at 180 °C for 12 h. After cooling down to room temperature naturally, the CoFe$_2$O$_4$/rGO hydrogels were rinsed with deionized water several times. For further characterization, freeze-drying technology under vacuum was employed to obtain aerogels. Four different CoFe$_2$O$_4$/rGO hybrid hydrogels were

prepared by changing the concentration of the GO precursor solution (2, 3, 3.5 and 4 mg mL^{-1}). For comparison, a pure CoFe$_2$O$_4$ sample was fabricated by following the same solvothermal process in the absence of GO. Meanwhile, a pure rGO hydrogel was prepared by using the same solvothermal process without inorganic metal salts as precursors.

Structural characterization

The morphology and microstructure of these samples were characterized using scanning electron microscopy (SEM, JEOL Hitachi S-4700, Japan) and high-resolution transmission electron microscopy (HRTEM, JEOL JEM200CX, JEOL). Powder X-ray diffraction (XRD, Bruker D8 Advance diffractometer with Cu-Kα radiation) experiments were performed to study the crystallographic information of the samples. X-ray photoelectron spectroscopy (XPS, Thermo Fisher Scientific, USA) was performed using an ESCALab MKII spectrometer with Al Kα (1.4866 keV) as the X-ray source. The specific Brunauer–Emmett–Teller (BET) surface areas of the hydrogels were measured by analyzing the nitrogen adsorption and desorption isotherms at −196 °C, obtained using a Micromeritics Model ASAP 2020 sorptometer.

Electrochemical measurements

Electrochemical properties were measured on an IVIUM electrochemical workstation in 6 M KOH solution as the electrolyte. A three-electrode system was employed, where Pt and Hg/HgO were used as the counter electrode and the reference electrode, respectively. The pure CoFe$_2$O$_4$ electrode was prepared by mixing 80 wt% CoFe$_2$O$_4$ powder with 10 wt% acetylene black and 10 wt% polytetrafluorene ethylene (PTFE) binder together. Then, drops of isopropyl alcohol were used to form slurries thoroughly. After drying in a vacuum oven at 60 °C for 8 h, the mixture was pressed onto nickel foam current collectors (1 × 1 cm^2). The CoFe$_2$O$_4$/rGO hybrid hydrogel electrode was prepared by cutting a piece of freeze-dried hydrogel, and then the patch was pressed onto the nickel foam current collectors (1 × 1 cm^2). Cyclic voltammetry (CV) and galvanostatic charge/discharge (GCD) measurements were carried out to test the electrochemical properties of the as-prepared electrodes. Electrochemical impedance spectroscopy (EIS) was preformed over a frequency range from 10^5 to 0.01 Hz at an amplitude of 5 mV. The capacitive performance of the electrodes in a two-electrode configuration was also assessed using CV and GCD, and a LAND battery system was used to examine the cycling stability. A battery-capacitor hybrid device was fabricated using CoFe$_2$O$_4$/rGO hybrid hydrogel as the positive electrode and rGO hydrogel as the negative electrode. The capability of the hybrid devices (CoFe$_2$O$_4$/rGO//rGO) (two single devices were connected in series) was evaluated by powering a light-emitting-diode (LED 3 V, 0.06 W).

Results and discussion

Structural characterization

The morphology and crystalline structure of the CoFe$_2$O$_4$/rGO hybrid hydrogel were investigated by SEM and XRD. Fig. 1a and
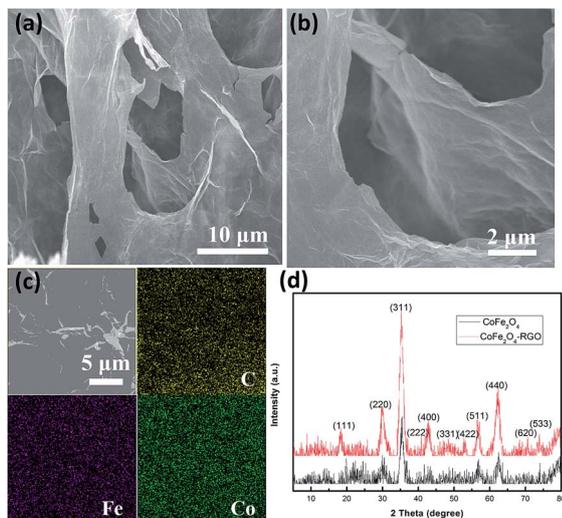
Fig. 1 (a and b) SEM images, and (c) elemental mapping of the CoFe$_2$O$_4$/rGO hybrid hydrogel. (d) XRD patterns of the pure CoFe$_2$O$_4$ and CoFe$_2$O$_4$/rGO hybrid hydrogel.

Fig. 2 (a and b) TEM images, (c) HR-TEM image and (d) EDX spectrum of the CoFe$_2$O$_4$/rGO hybrid hydrogel.

b show the SEM images of the CoFe$_2$O$_4$/rGO hybrid hydrogel after freeze-drying treatment under vacuum, displaying a 3D porous network with pore sizes ranging from sub-micrometers to several micrometers. This network is beneficial for enhancing the electrochemical properties, as it not only provides an efficient pathway for electron transport but also reduces the ion diffusion resistance of the electrolyte for charge storage reactions.[36,38] In addition, the 3D porous network provides abundant active sites to load CoFe$_2$O$_4$ nanoparticles. As shown in the elemental mapping images (Fig. 1c), C, Fe and Co are uniformly distributed in the composite, suggesting that the CoFe$_2$O$_4$ nanoparticles are homogeneously dispersed on the surface of the graphene sheets. Fig. 1d depicts the XRD patterns of the pure CoFe$_2$O$_4$ and the CoFe$_2$O$_4$/rGO hybrid, and the characteristic diffraction peaks at 18.3°, 30.1°, 35.4°, 37.1°, 43.1°, 53.4°, 57.0°, 62.6° and 74.0° can be assigned to the (111), (220), (311), (222), (400), (422), (511), (440) and (533) crystal planes of cubic spinel CoFe$_2$O$_4$ (JCPDS no. 22-1086), respectively.[44] After forming a composite with rGO, the highly crystalline nature of the CoFe$_2$O$_4$/rGO hybrid sample did not change. However, the conventional graphene-sheet stacking peak at $2\theta = 24.5°$ assigned to the (002) plane cannot be obviously seen, indicating that the graphene sheets might be restacked during the reduction process, resulting in the amorphous nature.[26]

To further investigate the details of the morphology and composition, TEM, HRTEM and EDX were employed. The TEM images (Fig. 2a and b) confirm that the CoFe$_2$O$_4$ nanoparticles are well-dispersed and firmly anchored on the graphene sheets. The HRTEM image in Fig. 2c reveals that the clear lattice fringe with an interplanar spacing of 0.25 nm corresponds well to the (311) plane of CoFe$_2$O$_4$. The EDX results (Fig. 2d) show the elements Co, Fe, O and C, which are in accordance with the nanocomposite and a Co/Fe atom ratio of about 1 : 2, further demonstrating the successful synthesis of the CoFe$_2$O$_4$/rGO hybrid hydrogel.
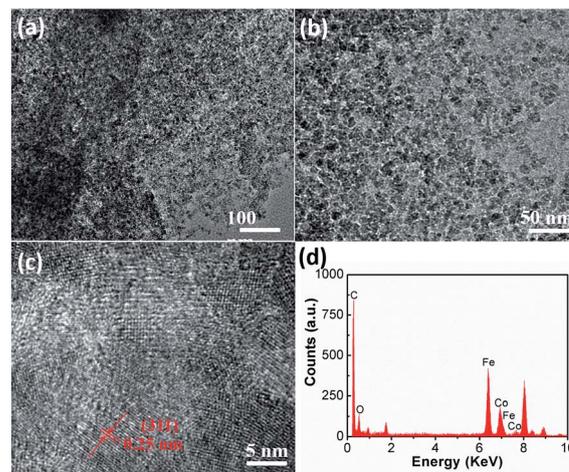
The chemical structure and valence states were studied using X-ray photoelectron spectroscopy (XPS) as shown in Fig. 3. The survey scan XPS spectrum of the CoFe$_2$O$_4$/rGO composite shows the existence of the elements Fe, Co, C and O. The high-resolution C1 XPS spectrum in Fig. 3b demonstrates plenty of functional groups on the graphene sheets. For example, the C 1s peaks at 284.7 and 286.5 eV can be attributed to the C=C and C–O groups of rGO in the composite, respectively.[42] The high resolution Co 2p spectrum (Fig. 3c) is deconvoluted into two spin–orbit doublets located at 781.6 and 796.7 eV, corresponding to the electronic states of Co 2p$_{3/2}$ and Co 2p$_{1/2}$, respectively, accompanied by two shakeup satellites centered at 784.8 and 803.8 eV. The main spin-energy separation of 15.1 eV is a signature of the Co^{2+} oxidation state.[45] As shown in Fig. 3d, in addition to the satellite peak at 716.7 eV, the peaks at 711.8 and 725.6 eV correspond to Fe 2p$_{3/2}$ and Fe 2p$_{1/2}$ spin–orbit peaks, respectively, which are attributed to the dominant states of
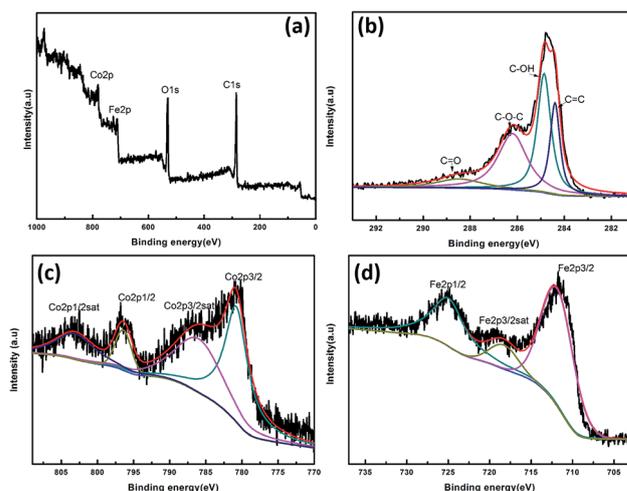

Fig. 3 XPS spectra of CoFe$_2$O$_4$/rGO composite: (a) survey scan, (b) C 1s, (c) Co 2p, and (d) Fe 2p spectrum.

(CoFe$_2$O$_4$/rGO(4)). It is noteworthy that the hybrid sample CoFe$_2$O$_4$/rGO(3.5) delivers the largest specific capacitance, which is in accordance with the area results from the CV curves in Fig. 6a. To further explore the electrochemical performance of the hybrid hydrogels, the CoFe$_2$O$_4$/rGO(3.5) sample was examined using CV at different scan rates and GCD at different current densities. Similarly, the CV curves measured at scan rates from 5 to 50 mV s^{-1}, as shown in Fig. 6c, exhibit a pair of symmetric redox peaks on each CV curve and the shapes are slightly different. The oxidation peak shifts to a higher potential, while the reduction peak shifts to a lower potential as the scan rate increases. A high symmetry at different current densities from 0.5 to 10 A g^{-1} is displayed in the GCD curves for the CoFe$_2$O$_4$/rGO(3.5) electrode (Fig. 6d). The specific capacitance values were calculated to be 356, 310.7, 298, 280, 265 and 244 F g^{-1} at current densities of 0.5, 1, 2, 3, 5 and 10 A g^{-1}, respectively. The hybrid hydrogel electrode maintains capacitance retention as high as 68.5% after increasing the current density 20-fold, indicating good rate capability.

The comparison of the specific capacitance for different composite samples with various current densities is plotted in Fig. 7a. With increasing current density, the specific capacitance for all the electrodes decreases gradually. This phenomenon is possibly attributed to the insufficient electroactive material involved in the faradaic reactions at higher current densities. These samples follow the trend: CoFe$_2$O$_4$/rGO(3.5) > CoFe$_2$O$_4$/rGO(3) > CoFe$_2$O$_4$/rGO(4) > rGO > CoFe$_2$O$_4$/rGO(2) > CoFe$_2$O$_4$, which is in good agreement with the results in Fig. 6a and b. This indicates that the introduction of an appropriate amount of rGO into CoFe$_2$O$_4$ nanoparticles is helpful for enhancing the specific capacitance. Meanwhile, varying the loading amount of the excellent conductive material rGO greatly affects the electrical conductivity of the composites, as indicated in the EIS spectra in Fig. 7b. The Nyquist plots for all the electrode samples display a depressed semicircle in the high-frequency region, corresponding to the charge transfer resistance, and a straight line in the low-frequency region, reflecting the diffusion of the electroactive species. The CoFe$_2$O$_4$/rGO(3.5)
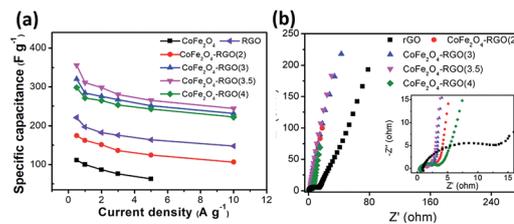
Fig. 7 (a) Comparison of specific capacitance at different current densities and (b) Nyquist plots for different electrodes.

electrode demonstrates the smallest semicircles, suggesting that it has the smallest charge transfer resistance, thus leading to the largest specific capacitance.

To further investigate the electrochemical properties of the CoFe$_2$O$_4$/rGO hybrid hydrogel electrodes in a full-cell configuration, an electrochemical energy storage device was assembled using the optimal CoFe$_2$O$_4$/rGO(3.5) sample as the positive electrode and the reduced graphene oxide (rGO) hydrogel as the negative electrode. To balance the charge storage between the positive electrode and negative electrode, the masses of the two electrodes were calculated according to eqn (3):

$$\frac{m^+}{m^-} = \frac{(C_{S-} \times \Delta \nu_-)}{(C_{S+} \times \Delta \nu_+)} \tag{3}$$
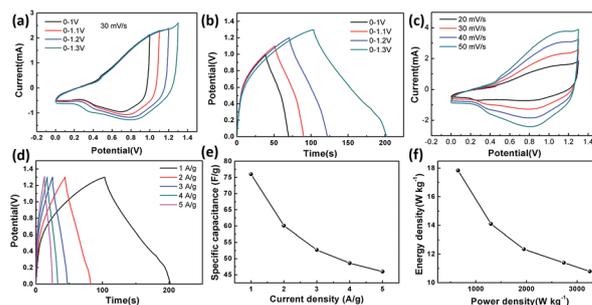
Fig. 8 The electrochemical properties of the CoFe$_2$O$_4$/rGO//rGO hybrid device in a two-electrode cell. (a) CV curves at different potential windows. (b) GCD curves at a current density of 1 A g^{-1}. (c) CV curves at different scan rates. (d) GCD curves at different current densities. (e) Specific capacitance at different current densities. (f) Ragone plots.
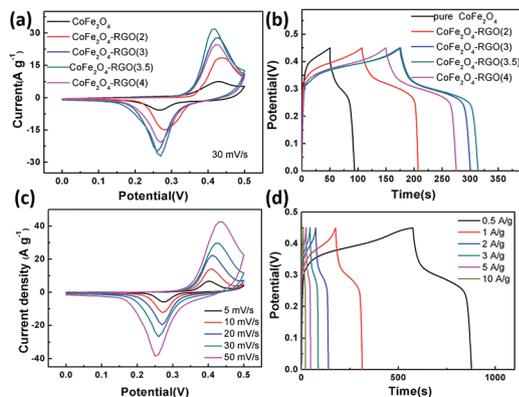
Fig. 6 (a) CV curves at a scan rate of 30 mV s^{-1}, and (b) GCD curves at a current density of 1 A g^{-1} for the different electrodes. (c) CV curves at different scan rates, and (d) GCD curves at different current densities ranging from 0.5 to 10 A g^{-1} for the CoFe$_2$O$_4$–rGO(3.5) sample.
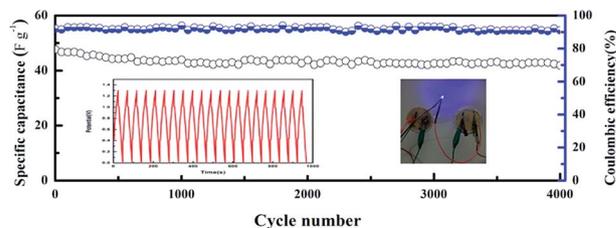
Fig. 9 Cycling performance and coulombic efficiency at 5 A g^{-1}. The inset on the left shows the GCD curves for the first 20 cycles, while the inset on the right shows the photograph of an LED powered by two CoFe$_2$O$_4$/rGO//rGO hybrid devices connected in series.

Table 1 Comparison of the electrochemical performances of CoFe$_2$O$_4$/rGO hybrid hydrogels with other related electrode materials in the literature

Electrode materials	Methods	Specific capacitance	Capacity retention	Ref.
CoFe$_2$O$_4$/rGO	Co-precipitation	123.2 F g^{-1} (5 mA cm^{-2})	78.1% (1000 cycles)	30
CoFe$_2$O$_4$/graphene	Hydrothermal	166.5 C g^{-1} (0.5 A g^{-1})	79.3% (5000 cycles)	48
FeMnO$_3$/graphene	Thermal treatment	189 F g^{-1} (0.5 A g^{-1})	75.4% (1500 cycles)	52
NiCo$_2$O$_4$/CNTs	Thermal treatment	210 F g^{-1} (2 A g^{-1})	92.7% (2500 cycles)	53
CoFe$_2$O$_4$/rGO	Solution combustion	195 F g^{-1} (1 mV s^{-1})	66.7% (3000 cycles)	54
MnFe$_2$O$_4$/carbon black/polyaniline	Hydrothermal & polymerization	205 F g^{-1} (0.5 A g^{-1})	80% (10 000 cycles)	55
CoFe$_2$O$_4$/rGO/polyaniline	Solution combustion & polymerization	257 F g^{-1} (1 mV s^{-1})	—	56
NiFe$_2$O$_4$/rGO	Hydrothermal	345 F g^{-1} (1 A g^{-1})	60% (300 cycles)	57
CoFe$_2$O$_4$/rGO hydrogel	**Hydrothermal**	**356 F g^{-1} (0.5 A g^{-1})**	**87% (4000 cycles)**	**This work**

where m^+ and m^- are the masses of the positive and negative electrodes (g), respectively, and the specific capacitance C_{S-}, C_{S+} (F g^{-1}), and the voltage range $\Delta\nu_-$, $\Delta\nu_+$ (V) are for the negative and positive electrodes, respectively.[39]

The specific capacitance of CoFe$_2$O$_4$/rGO(3.5) is 310.7 F g^{-1}, while that of rGO is 197.5 F g^{-1} at a current density of 1 A g^{-1} (Fig. 7a). The potential windows of the CoFe$_2$O$_4$/rGO hybrid electrode and the pure rGO electrode are 0–0.5 V and −0.8–0 V, respectively. Therefore, the mass ratio $\left(\dfrac{m^+}{m^-}\right)$ between the two electrodes is 1.02. Fig. 8a displays the CoFe$_2$O$_4$/rGO//rGO electrochemical energy storage device in 6 M KOH solution with different potential windows varying from 0–1 V to 0–1.3 V at a scan rate of 30 mV s^{-1}. When the cell voltage reaches 1.3 V, there is no obvious change of anodic current, indicating that the cell electrolyte is stable at 1.3 V. The GCD curves of the hybrid device under different voltage ranges at 1 A g^{-1} are revealed in Fig. 8b. The curves of each GCD exhibit a good symmetrical shape. In particular, the potential window of the hybrid device is beyond the thermodynamic limit of ~1.2 V and thus greatly improves the energy density.[44,48,52] The potential window of 0–1.3 V was chosen for further investigation with CV and GCD tests. Fig. 8c shows the CV curves of the CoFe$_2$O$_4$/rGO//rGO hybrid device at scan rates varying from 20 to 50 mV s^{-1}. With increasing scan rate, the peak current increases. Moreover, the CV curves show two relatively weak redox peaks, revealing synergistic contributions from both the electric double-layer capacitance and the pseudocapacitance. The specific capacitances calculated from the GCD curves in Fig. 8d of the hybrid device are 76, 60.1, 52.7, 48.6 and 46 F g^{-1} at a current density of 1, 2, 3, 4 and 5 A g^{-1}, respectively (Fig. 8e). The energy density and power density were calculated according to eqn (4) and (5), respectively:

$$E = \frac{1}{2}C \times \Delta V^2 \tag{4}$$

$$P = \frac{E}{\Delta t} \tag{5}$$

where C is the specific capacitance, ΔV is the potential window, and Δt is the discharge time. The hybrid device delivers a maximum energy density of 17.84 W h kg^{-1} at a power density of 650 W kg^{-1} and a maximum power density of 3250 W kg^{-1} at an energy density of 10.8 W h kg^{-1} (Fig. 8f).

The cycling performance of the CoFe$_2$O$_4$/rGO//rGO hybrid device was also tested for charge–discharge cycles at a high current density of 5 A g^{-1}, and the specific capacitance was found to still be stable at 40.2 F g^{-1} with 87% retention of the initial value after 4000 cycles (Fig. 9). Additionally, the coulombic efficiency remains near 92% after 4000 cycles, further confirming the excellent cycling stability and reversibility of the faradic reactions. Table 1 lists the main electrochemical parameters of the CoFe$_2$O$_4$/rGO hybrid hydrogel electrode compared with the related electrode materials in the literature. It is obvious that the specific capacitance of the novel hydrogel electrode material is comparable with the best values obtained for related CoFe$_2$O$_4$-based electrode materials that possess excellent stability. Moreover, two CoFe$_2$O$_4$/rGO//rGO devices connected in series can power a light emitting diode (LED) with a voltage of 3.0 V for several seconds (inset (right) in Fig. 9), confirming their promising application in energy storage devices.

Conclusions

In summary, we have presented a scalable strategy to construct a unique architecture comprising 3D porous rGO hydrogel-supported CoFe$_2$O$_4$ nanoparticles, through a facile one-pot solvothermal process. The as-prepared CoFe$_2$O$_4$ nanoparticles are evenly distributed on the surfaces of graphene sheets. When used as a binder-free supercapacitor electrode material, CoFe$_2$O$_4$/rGO synthesized using 3.5 mg mL^{-1} GO precursor solution shows a high capacitance of up to 356 F g^{-1} at 0.5 A g^{-1}, which is 3.2 times higher than the pure CoFe$_2$O$_4$ nanoparticle electrode, due to the large specific surface area and excellent electric conductivity. Moreover, the CoFe$_2$O$_4$/rGO//rGO electrochemical energy storage device exhibits a high energy density of 17.84 W h kg^{-1} at a power density of 650 W kg^{-1} and 87% capacitance retention at 5 A g^{-1} after 4000 cycles. The excellent electrochemical performance indicates that CoFe$_2$O$_4$/rGO hybrid hydrogels hold great promise for high-performance energy storage devices.

Conflicts of interest

There are no conflicts to declare.

Acknowledgements

References

1 G. P. Wang, L. Zhang and J. J. Zhang, *Chem. Soc. Rev.*, 2012, **41**, 797–828.

2 M. F. El-Kady, V. Strong, S. Dubin and R. B. Kaner, *Science*, 2012, **335**, 1326–1330.

3 H. Zheng, F. Tang, Y. Jia, L. Wang, Y. Chen, M. Lim, L. Zhang and G. Lu, *Carbon*, 2009, **47**, 1534–1542.

4 P. Simon and Y. Gogotsi, *Nat. Mater.*, 2008, **7**, 845–854.

5 H. Ma, J. He, D. Xiong, J. Wu, Q. Li, D. Vinaya and Y. Zhao, *ACS Appl. Mater. Interfaces*, 2016, **8**, 1992.

6 R. R. Salunkhe, K. Jang, S. W. Lee, S. Yu and H. Ahn, *J. Mater. Chem.*, 2012, **22**, 21630–21635.

7 Z. Q. Peng, S. A. Freunberger, Y. H. Chen and P. G. Bruce, *Science*, 2012, **337**, 563–566.

8 J. S. Lee, S. T. Kim, R. Cao, N. S. Choi, M. Liu, K. T. Lee and J. Cho, *Adv. Energy Mater.*, 2011, **1**, 34–50.

9 H. Zheng, F. Tang, M. Lim, A. Mukherji, X. Yan, L. Wang and G. Q. Lu, *J. Power Sources*, 2010, **195**, 680–683.

10 M. Wang, F. Jin, X. Zhang, J. Wang, S. Huang, X. Zhang, S. Mu, Y. Zhao and Y. Zhao, *ACS Sustainable Chem. Eng.*, 2017, **5**, 5679–5685.

11 J. Shen, X. Li, L. Wan, K. Liang, B. K. Tay, L. Kong and X. Yan, *ACS Appl. Mater. Interfaces*, 2017, **9**, 668–676.

12 B. Wang, J. S. Chen, Z. Wang, S. Madhavi and X. W. Lou, *Adv. Energy Mater.*, 2012, **2**, 1188–1192.

13 J. Di, X. Fu, H. Zheng and Y. Jia, *J. Nanopart. Res.*, 2015, **17**, 1–12.

14 L. Zheng, Y. Dong, H. Bian, C. Lee, J. Lu and Y. Y. Li, *Electrochim. Acta*, 2016, **203**, 257–264.

15 L. Zheng, C. Wang, Y. Dong, H. Bian, T. F. Hung, J. Lu and Y. Y. Li, *Appl. Surf. Sci.*, 2016, **362**, 399–405.

16 S. Chen, G. Yang, Y. Jia and H. Zheng, *J. Mater. Chem. A*, 2017, **5**, 1028–1034.

17 X. Chen, X. H. Chen, F. Q. Zhang, Z. Yang and S. M. Huang, *J. Power Sources*, 2013, **243**, 555–561.

18 Y. Zhao, H. Ma, S. Huang, X. Zhang, M. Xia, Y. Tang and Z. F. Ma, *ACS Appl. Mater. Interfaces*, 2016, **8**, 22997.

19 S. Huang, Z. Li, B. Wang, J. Zhang, Z. Peng, R. Qi, J. Wang and Y. Zhao, *Adv. Funct. Mater.*, 2018, 1706294.

20 Z. Wang, W. Jia, M. Jiang, C. Chen and Y. Li, *Nano Res.*, 2016, **9**, 2026–2033.

21 S. Chen, G. Yang and H. Zheng, *Electrochim. Acta*, 2016, **220**, 296–303.

22 C. Vidal-Abarca, P. Lavela and J. L. Tirado, *J. Power Sources*, 2011, **196**, 6978–6981.

23 V. S. Kumbhar, A. D. Jagadale, N. M. Shinde and C. D. Lokhande, *Appl. Surf. Sci.*, 2012, **259**, 39–43.

24 P. Xiong, H. J. Huang and X. Wang, *J. Power Sources*, 2014, **245**, 937–946.

25 H. Fu, Z. J. Du, W. Zou, H. Q. Li and C. Zhang, *Carbon*, 2013, **65**, 112–123.

26 H. Xia, D. D. Zhu, Y. S. Fu and X. Wang, *Electrochim. Acta*, 2012, **83**, 166–174.

27 X. Zhang, X. Zhang, X. G. Wang, Z. J. Xie and Z. Zhou, *J. Mater. Chem. A*, 2016, **4**, 9390–9393.

28 Z. L. Zhang, Y. H. Wang, M. J. Zhang, Q. Q. Tan, X. Lv, Z. Y. Zhong and F. B. Su, *J. Mater. Chem. A*, 2013, **1**, 7444–7450.

29 R. Wang and X. Yan, *Sci. Rep.*, 2014, **4**, 3712.

30 P. He, K. Yang, W. Wang, F. Dong, L. Du and Y. Deng, *Russ. J. Electrochem.*, 2013, **49**, 359–364.

31 J. Zhu, D. Yang, Z. Yin, Q. Yan and H. Zhang, *Small*, 2014, **10**, 3480.

32 L. L. Jiang and Z. J. Fan, *Nanoscale*, 2014, **6**, 1922–1945.

33 Y. Zhao, S. Huang, M. Xia, S. Rehman, S. Mu, Z. Kou, Z. Zhang, Z. Chen, F. Gao and Y. Hou, *Nano Energy*, 2016, **28**, 346–355.

34 Y. Zhao, W. Ran, J. He, Y. Huang, Z. Liu, W. Liu, Y. Tang, L. Zhang, D. Gao and F. Gao, *Small*, 2015, **11**, 1310–1319.

35 Y. Liu, R. Wang and X. Yan, *Sci. Rep.*, 2015, **5**, 11095.

36 Y. Xu, K. Sheng, C. Li and G. Shi, *ACS Nano*, 2010, **4**, 4324–4330.

37 S. Zhu, M. Wu, M. H. Ge, H. Zhang, S. K. Li and C. H. Li, *J. Power Sources*, 2016, **306**, 593–601.

38 R. H. Wang, C. H. Xu and J. M. Lee, *Nano Energy*, 2016, **19**, 210–221.

39 S. Zhu, H. Zhang, P. Chen, L. H. Nie, C. H. Li and S. K. Li, *J. Mater. Chem. A*, 2015, **3**, 1540–1548.

40 H. Zheng, G. Yang, S. Chen and Y. Jia, *ChemElectroChem*, 2017, **4**, 577–584.

41 H. W. Wang, H. Yi, X. Chen and X. F. Wang, *J. Mater. Chem. A*, 2014, **2**, 1165–1173.

42 S. S. Wu, W. F. Chen and L. F. Yan, *J. Mater. Chem. A*, 2014, **2**, 2765–2772.

43 W. S. Hummers and R. E. Offeman, *J. Am. Chem. Soc.*, 1958, **80**, 1339.

44 H. C. Gao, F. Xiao, C. B. Ching and H. W. Duan, *ACS Appl. Mater. Interfaces*, 2012, **4**, 2801–2810.

45 S. Chen, G. Yang, Y. Jia and H. Zheng, *ChemElectroChem*, 2016, **3**, 1490–1496.

46 S. Nappini, E. Magnano, F. Bondino, I. Pis, A. Barla, E. Fantechi, F. Pineider, C. Sangregorio, L. Vaccari, L. Venturelli and P. Baglioni, *J. Phys. Chem. C*, 2015, **119**, 25529–25541.

47 S. Liu, W. Bian, Z. Yang, J. Tian, C. Jin, M. Shen, Z. Zhou and R. Yang, *J. Mater. Chem. A*, 2014, **2**, 18012–18017.

48 P. Liu, H. Chen, X. Chang, Y. Xue, J. Zhou, Z. Zhao, H. Lin and S. Han, *Electrochim. Acta*, 2017, **231**, 565–574.

49 A. C. Ferrari, J. C. Meyer, V. Scardaci, C. Casiraghi, M. Lazzeri, F. Mauri, S. Piscanec, D. Jiang, K. S. Novoselov, S. Roth and A. K. Geim, *Phys. Rev. Lett.*, 2006, **97**, 187401.

50 I. Calizo, A. A. Balandin, W. Bao, F. Miao and C. N. Lau, *Nano Lett.*, 2007, **7**, 2645.

51 K. Parvez, Z. S. Wu, R. Li, X. Liu, R. Graf, X. Feng and K. Müllen, *J. Am. Chem. Soc.*, 2014, **136**, 6083.

52 M. Li, W. Xu, W. Wang, Y. Liu, B. Cui and X. Guo, *J. Power Sources*, 2014, **248**, 465–473.

53 M. Shahraki, S. Elyasi, H. Heydari and N. Dalir, *J. Electron. Mater.*, 2017, **46**, 4948–4954.

54 K. V. Sankar, R. K. Selvan and D. Meyrick, *RSC Adv.*, 2015, **5**, 99959–99967.

55 D. Zha, P. Xiong and X. Wang, *Electrochim. Acta*, 2015, **185**, 218–228.

56 K. Vijaya Sankar and R. Kalai Selvan, *Electrochim. Acta*, 2016, **213**, 469–481.

57 Z. Wang, X. Zhang, Y. Li, Z. Liu and Z. Hao, *J. Mater. Chem. A*, 2013, **1**, 6393–6399.